CHEMISTRY OF MATERIALS
Article

Chem. Mater. **2010,** *22,* 6065–6074 6065
DOI:10.1021/cm101418z

Hierarchical Porous Zeolite Composite with a Core−Shell Structure Fabricated Using β-Zeolite Crystals as Nutrients as Well as Cores

Jiajun Zheng,[†] Qinghu Zeng,[†] Yanyu Zhang,[†] Yan Wang,[†] Jinghong Ma,[†] Xiwen Zhang,[‡] Wanfu Sun,[‡] and Ruifeng Li*[,†]

[†]*Key Laboratory of Coal Science and Technology MOE, Institute of Special Chemicals, Taiyuan University of Technology, Taiyuan 030024, China, and* [‡]*Fushun Research Institute of Petroleum and Petrochemicals, SINOPEC, Fushun 113001, China*

Received May 21, 2010. Revised Manuscript Received September 29, 2010

A hierarchical porous zeolite composite possessing β-zeolite cores and Y-zeolite polycrystalline shells (denoted as BFZ) is synthesized by a two-step hydrothermal crystallization procedure and characterized by X-ray diffraction (XRD), N_2 adsorption−desorption, scanning electron microscopy (SEM), high resolution transmission electron microscopy (HRTEM), selected area electron diffraction (SAED), energy-dispersive spectrometry (EDS), NMR, intelligent gravimetric analyzer (IGA), and in situ infrared (IR) spectrometry of pyridine. The results show that a hierarchical pore structure with the pore size centered around 6.9, 10.3, and 16 nm is created in the composite. A more than 2 orders of magnitude gas transport improvement is, therefore, achieved in the composite as compared with the corresponding physical mixture. The conversion of liquid-phase hydrogenation of benzene over H-BFZ supported by 3 wt % Ru is much higher than those over H-Y or H-β-zeolites supported by the same Ru loading due to the improved diffusion and acid accessibility as well as the enhanced Ru dispersion because of the introduction of hierarchical pores.

1. Introduction

Zeolites are widely used in heterogeneous catalysis as well as in the separation and purification fields due to their uniform, small pore size, high internal surface area, flexible frameworks, and controlled chemistry.[1] However, their use was hampered by their small microporous channels, which are subject to diffusional limitations on reaction rates[2−6] because of the similarity between the size of the involved guest molecules and the micropore diameter. For a given zeolite framework, the basic strategy to change the diffusion path length was altering crystal size and morphology using particular crystallization conditions. Aiming at shorter diffusion path lengths in micropores of existing zeolites, "hierarchical" systems have been developed and have attracted rapidly growing attention. In zeolites, this can be attained by decreasing the crystal size or by introducing an additional (meso)pore system within an individual zeolite crystal.[2]

In the past decades, there have been a considerable number of attempts to improve the micropore diffusion in zeolites by adjusting their crystal sizes to nanoscale ranges, which can be achieved by adding growth inhibitors, by increasing the supersaturation, or by quenching crystallization.[2] However, none of these attempts had produced an easy means of controlling the crystal size,[7] and separation of the small zeolite crystals from the reaction mixture by filtration was difficult owing to the colloidal properties of these materials,[2] which severely hindered their practical applications. Moreover, the volume and surface area of the micropores in zeolites was decreased because the ordering of the three-dimensional network of the zeolite particles deteriorated when the crystal size decreased to the nanocrystalline region.[6]

Another alternative approach to alleviate diffusion limitation is to insert larger pores into the zeolite particles, since the diffusion in mesopores is several orders of magnitude faster than in micropores.[2] Synthesis of new zeolite materials containing considerable intracrystalline mesopores that provide a better diffusion transport has recently attracted attention of many researchers in the field.[8−10] The created mesoporosity facilitated physical transport and led to a more effective use of these materials.[11−13] In this way, the

*Corresponding author. E-mail: rfli@tyut.edu.cn. Fax: +86 351 6010121. Address: Institute of Special Chemicals, Taiyuan University of Technology, 79# West Yingze Street, Taiyuan 030024, China.

(1) Tao, Y.; Kanoh, H.; Abrams, L.; Kaneko, K. *Chem. Rev.* **2006**, *106*, 896.
(2) Pérez-Ramírez, J; Christensen, C. H.; Egeblad, K.; Christensend, C. H.; Groen, J. C. *Chem. Soc. Rev.* **2008**, *37*, 2530.
(3) Egeblad, K.; Christensen, C. H.; Kustova., M.; Christensen, C. H. *Chem. Mater.* **2008**, *20*, 946.
(4) van Donk, S.; Broersma, A.; Gijzeman, O. L. J.; van Bokhoven, J. A.; Bitter, J. H.; de Jong, K. P. *J. Catal.* **2001**, *204*, 272.
(5) van Donk, S.; Janssen, A. H.; Bitter, J. H.; de Jong, K. P. *Catal. Rev. Sci. Eng.* **2003**, *45*, 297.
(6) Tao, Y.; Kanoh, H.; Kaneko, K. *Langmuir* **2005**, *21*, 504.
(7) Hartmann, M. *Angew. Chem., Int. Ed.* **2004**, *43*, 5880.
(8) Wang, H.; Pinnavaia, T. J. *Angew. Chem., Int. Ed.* **2006**, *45*, 7603.
(9) Serrano, D. P.; Aguado, J.; Escola, J. M.; Rodríguez, J. M.; Peral, A. *Chem. Mater.* **2006**, *18*, 2462.
(10) Yang, Z.; Xia, Y.; Mokaya, R. *Adv. Mater.* **2004**, *16*, 727.
(11) Groen, J. C.; Bach, T.; Ziese, U.; van Donk, A. M. P.; de Jong, K. P.; Moulijn, J. A.; Pérez-Ramírez, J. *J. A.m. Chem. Soc.* **2005**, *127*, 10792.
(12) Groen, J. C.; Zhu, W.; Brouwer, S.; Huynink, S. J.; Kapteijn, F.; Moulijn, J. A.; Pérez-Ramírez, J. *J. A.m. Chem. Soc.* **2007**, *129*, 355.
(13) Zheng, J.; Zeng, Q.; Ma, J.; Zhang, X.; Sun, W.; Li, R. *Chem. Lett.* **2010**, *39*, 330.

Published on Web 10/21/2010

micropores of the zeolite were effectively shortened and their molecular accessibility was largely enhanced.[14,15] Combination of micropores with mesopores in one crystal can be undertaken by post-treatment[11,12,16−20] or a template approaches.[3,21−25]The created mesopores in ZSM-5 zeolite crystals by the alkali-leaching approach afforded a more than 2 orders of magnitude gas transport improvement as compared with the untreated samples owing to the shortened microporous channels.[12] The hydroisomerization activity on Pt/H-mordenite was much higher than on untreated Pt/H-mordenite, because it gave rise to an acceleration of the uptake of *n*-hexane under reaction conditions due to a shorter intracrystalline diffusion path length resulting from the mesoporous structure created by the acid-leaching approach.[4] In recent years, using the template method to synthesize mesoporous zeolite has proven to be very effective. Christensen et al.[2,3] had categorized the templating approaches available to synthesize hierarchical zeolites as solid templating, supramolecular templating, and indirect templating. Jacobsen and co-workers[21,22] synthesized mesoporous zeolite crystals using a carbon matrix with a mesopore system or multiwall carbon nanotubes as the mesopore-forming agents. Tao et al[23,24] reported a method of preparing zeolite ZSM-5 monolith with a bimodal pore structure of uniform mesopores (average diameter: 11 nm) by the templating method using a carbon aerogel of uniform mesopores. The zeolite crystals were nucleated within the three-dimensional mesoporous system of carbon aerogels. Removal of the carbon aerogels by burning led to monolithic zeolite with a mesoporous system. Mesoporous NaY synthesized with the carbon aerogel templating was also reported in the opened literature.[25]

Despite that the embedding of carbon nanoparticles and certain polymers into zeolite crystals during synthesis had been shown an effective means of generating intracrystalline mesopores, these templating methods provided much better control of pore size than conventional steaming and chemical leaching approaches to mesopore formation in zeolites.[5] However, particle templates are difficult to be applied in industry because they typically afford average pore sizes that are too large (≥10 nm) and pore size distributions that are too broad (>10 nm widths at half-maximum) for catalytic reactions with high product selectivity as well as the use of expensive template.[2]

In the present paper, we report a new method for synthesizing hierarchical porous zeolite composite with a core−shell structure by employing the as-synthesized β-zeolite as silica source as well as the core. The low stability of the β-framework in alkaline solutions will result in the silicon extraction during the second-step synthesis[26] and, therefore, provide the silicon species that Y-zeolite needs. The interaction between the aluminum species from the synthesis solution and the silicon species extracted from β-zeolite crystal promotes the growth of Y-zeolite. These lead to on the one hand the formation of the composite zeolite and on the other hand the introduction of a mesopore system throughout the zeolite crystals. We selected isopropylbenzene as a probe to make a comparative study on the uptakes in the composite and the corresponding mixture samples so as to verify whether an improved transport properties in the core−shell zeolite composite occurs. The effects of hierarchical pores on the performances of the as-synthesized zeolite composite samples were evaluated during the liquid-phase hydrogenation of benzene.

2. Experimental Section

β-Zeolite was first prepared with the molar composition of the gel: $2.2Na_2O/20SiO_2/Al_2O_3/4.6(TEA)_2O/4.6(NH_4)_2O/440H_2O$. An aliquot of 2.28 g of sodium aluminate (41 wt % Al_2O_3, 35 wt % Na_2O), 17.58 g of tetraethylammonium bromide (TEABr), and 0.5 g of sodium hydroxide (96 wt %) were mixed in 34 mL of water and 5.8 mL of ammonia−water (27 wt %) to form a clear solution, and then, 32 mL of silica sol (29 wt %) was slowly added to the solution with vigorous stirring. The mixture was stirred at room temperature for 2 h and transferred into a 100 mL autoclave and kept at 413 K for 240 h without stirring. The reacted mixture containing the presynthesized β-zeolite was directly used in the second-step synthesis. An aliquot of 4.25 g of sodium aluminate, 1.60 g of sodium hydroxide, and 3 mL of seeds of Y-zeolite were added to the reacted mixture and stirred for 2 h at room temperature. Y-Zeolite seeds were prepared according to the molar composition described next: $13Na_2O/15\ SiO_2/Al_2O_3/320\ H_2O$. The new mixture was then loaded into an autoclave for hydrothermal treatment at 363 K for 12−36 h under autogenous pressure. The as-synthesized solid product was recovered by filtration, washed with water, dried in air at 373 K overnight, and denoted as BFZ-*m* (*m*: stands for the second-step hydrothermally treatment time, hour). A physical mixture of β- and Y-zeolites was prepared and denoted as B + F.

The X-ray diffraction (XRD) patterns were recorded using a Rigaku Dmax/2500 X-ray diffractometer, which employed Ni-filtered Cu Kα radiation and was operated at 40 kV and 80 mA. A working plot can be obtained by plotting the intensity of the diffraction peak at $2\theta = 6.16$ versus the mass fraction of Y-zeolite by measuring a series of physical mixtures with known mass fractions of Y-zeolite. The mass fraction of Y-zeolite in the

(14) Ordomsky, V. V.; Murzin, V. Y.; Monakhova, Y. V.; Zubavichus, Y. V.; Knyazeva, E. E.; Nesterenko, N. S.; Ivqanova, I. I. *Microporous Mesoporous Mater*. **2007**, *105*, 101.
(15) Nesterenko, N. S.; Thibault-Starzyk, F.; Montouillout, V.; Yuschenko, V. V.; Fernandez, C.; Gilson, J.-P.; Fajula, F.; Ivanova, I. I. *Microporous Mesoporous Mater*. **2004**, *71*, 157.
(16) Tromp, M.; van Bokhoven, J. A.; Garriga Oostenbrink, M. T.; Bitter, J. H.; de Jong, K. P.; Koningsberger, D. C. *J. Catal*. **2000**, *190*, 209.
(17) Groen, J. C.; Peffer, L. A. A.; Moulijn, J. A.; Pérez-Ramírez, J. *Colloids Surf., A* **2004**, *241*, 53.
(18) Groen, J. C.; Moulijn, J. A.; Pérez-Ramírez, J. *Microporous Mesoporous Mater*. **2005**, *87*, 153.
(19) Groen, J. C.; Brückner, A.; Berrier, E.; Maldonado, L.; Moulijn, J. A.; Pérez-Ramírez, J. *J. Catal*. **2006**, *243*, 212.
(20) Groen, J. C.; Peffer, L. A. A.; Moulijn, J. A.; Pérez-Ramírez, J. *Chem.−Eur. J*. **2005**, *11*, 4983.
(21) Jacobsen, C. J. H.; Madsen, C.; Houzvicka, J.; Schmidt, I.; Carlsson, A. *J. Am. Chem. Soc*. **2000**, *122*, 7116.
(22) Schmidt, I.; Boisen, A.; Gustavsson, E.; Ståhl, K.; Pehrson, S.; Dahl, S.; Carlsson, A.; Jacobsen, C. J. H. *Chem. Mater*. **2001**, *13*, 4416.
(23) Tao, Y.; Kanoh, H.; Kaneko, K. *J. A.m. Chem. Soc*. **2003**, *125*, 6044.
(24) Tao, Y.; Hattori, Y.; Matumoto, A.; Kanoh, H.; Kaneko, K. *J. Phys. Chem. B* **2005**, *109*, 194.
(25) Tao, Y.; Kanoh, H.; Kaneko, K. *J. Phys. Chem. B* **2003**, *107*, 10974.
(26) Groen, J. C.; Abelló, S; Villaescusa, L. A; Pérez-Ramírez, J. *Microporous Mesoporous Mater*. **2008**, *114*, 93.

composite BFZ can be estimated from the intensity of the XRD diffraction peak at $2\theta = 6.16$, which is the characteristic peak of Y-zeolite.

Crystal size, morphology, mesoporosity of the composite BFZ, and the corresponding Y and β were investigated on a JSM-6301F scanning electron microscope; crystal faces and interface structure were studied on a JEM-200CX transmission electron microscopy (TEM) coupled with selected area electron diffraction (SAED) and energy dispersive analysis of X-rays (EDAX) spectroscopy. The particles were crushed by 3 MPa pressure prior the energy-dispersive spectrometry (EDS) analyses.

N_2 adsorption at 77 K was performed in a NOVA 1200e gas sorption analyzer to study the micro- and mesoporosity in the zeolite crystals. The mesopore size distribution was calculated using the Barret−Joyner−Halenda (BJH) pore size model applied to the adsorption branch of the isotherm. The microporous structure was obtained from the *t*-plot analysis of the adsorption branch of the isotherm.

Infrared spectra of pyridine adsorption were obtained on a SHIMADZU FTIR-8400 spectrometer. About 12 mg of sample was pressed into a self-supporting wafer of 10 mm in diameter. The wafer was first evacuated in situ in an infrared (IR) cell at 573 K for 2 h, and the IR spectra were recorded at room temperature. Pyridine was then introduced into the cell at room temperature until the saturated adsorption was reached. Finally, desorption of pyridine was performed at increasing temperatures under 3×10^{-3} Pa of pressure, and the spectra were recorded at various temperatures.

Isopropylbenzene diffusion kinetics in Na^+-form samples at 28 °C were investigated using a Hiden IGA 003 electronic microbalance. The catalyst was outgassed under a vacuum of $< 10^{-3}$ Pa at 673 K for more than 10 h prior to the adsorption measurement. The sample temperature was regulated to ±0.1 °C by a water bath. The pressure was determined using two high accuracy Baratron pressure transducers and increased step by step in order to obtain the entire equilibrium adsorption isotherm. For each step, the amount of isopropylbenzene (> 99% purity, Fluka, AG) introduced into the system was kept small enough in order to consider the diffusion an isothermal process.

The protonic form samples were impregnated (incipient wetness) with the required amount of $RuCl_3$ in an aqueous solution to prepare supported Ru catalysts; the Ru content in all catalysts was 3 wt %. The impregnated samples were washed free of chloride, dried at 383 K, and calcined at 673 K in air with a ramp of 0.5 K/min. After cooling in air, the calcined catalysts were reduced in flowing H_2 for 6 h at the same final temperature and heating rate prior to being tested. The experiments for benzene hydrogenation were performed in a 160 mL batch stirred reactor (Parr4842). Catalyst (0.05 g) was transferred into the reactor in which 40 mL of a 0.06 wt % solution of benzene dissolved in *n*-hexane had been introduced. The system was flushed and then pressurized by H_2 to the 4.0 MPa of operating pressure and simultaneously heated up to 40 °C of reaction temperature. The products were analyzed by GC equipped with a flame ionization detector (FID) and a column of polyglycol.

3. Results and Discussion

3.1. Synthesis and Characterization. The dissolution of the preformed β-crystals in basic medium is a key aspect to attain β(core)−Y(shell) composites. The low stability of the β-framework in alkaline solutions[26] can provide nutrients for the growth of Y-zeolite during the second-step synthesis. The interaction between the aluminum species from the synthesis solution and the silicon species extracted from β-zeolite crystal promotes the growth of Y-zeolite. Figure 1 shows the XRD patterns of the as-synthesized BFZ zeolite composite samples with the different second-step crystallization time. When the crystallization time was shorter than 12 h, the mass fraction of FAU zeolite phase in BFZ was very low because the time is not enough to provide solubilization of silicate to promote crystallization of Y-zeolite due to the silicon species can only be obtained from the depolymerization of β-zeolite. When the crystallization time was 18−28 h, a composite with different ratios of FAU to BEA was obtained. Perhaps the degradation of β-zeolite by the synthesis solution is such as to provide enough solubilized silicon species[27] to accelerate the growth of Y-zeolite. However, when the crystallization time was further prolonged, such as over 36 h, a product abundant in Y-zeolite commingled with P-type zeolite was obtained and the characteristic peaks of β-zeolite may completely disappear. Extensive dissolution of β-zeolite crystals makes the synthesis system deviate from the crystallization field of the given zeolite Y. As a consequence, zeolite composite BFZ is difficult to be formed. A 6 parallel-batch reactor was used to study the influence of the synthesis condition on the physicochemical properties of the composite zeolite and showed the reproducibility in the preparation of this composite material was good enough as the crystallization time was 18−28 h.

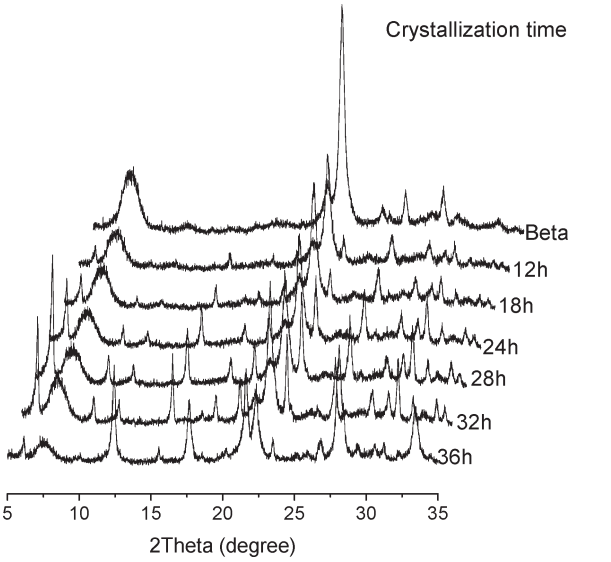

Figure 1. XRD patterns of the as-synthesized zeolite core−shell BFZ composite with different hydrothermal treatment time.

Crystal morphology of the zeolite composite BFZ differs from those of Y- or β-zeolites, as shown in Figure 2. Zeolite β and zeolite Y show the spherelike crystal particles and octahedral morphology, respectively. Both the sizes are about 1 μm, obviously smaller than that of the composite (about 2−4 μm). The relatively bigger crystals of the composite BFZ can be ascribed to the fact that Y-zeolite crystals were grown around β-zeolite particles.

(27) Zheng, J.; Ma, J.; Wang, Y.; Bai, Y.; Zhang, X.; Li, R. *Catal. Lett.* **2009**, *130*, 672.

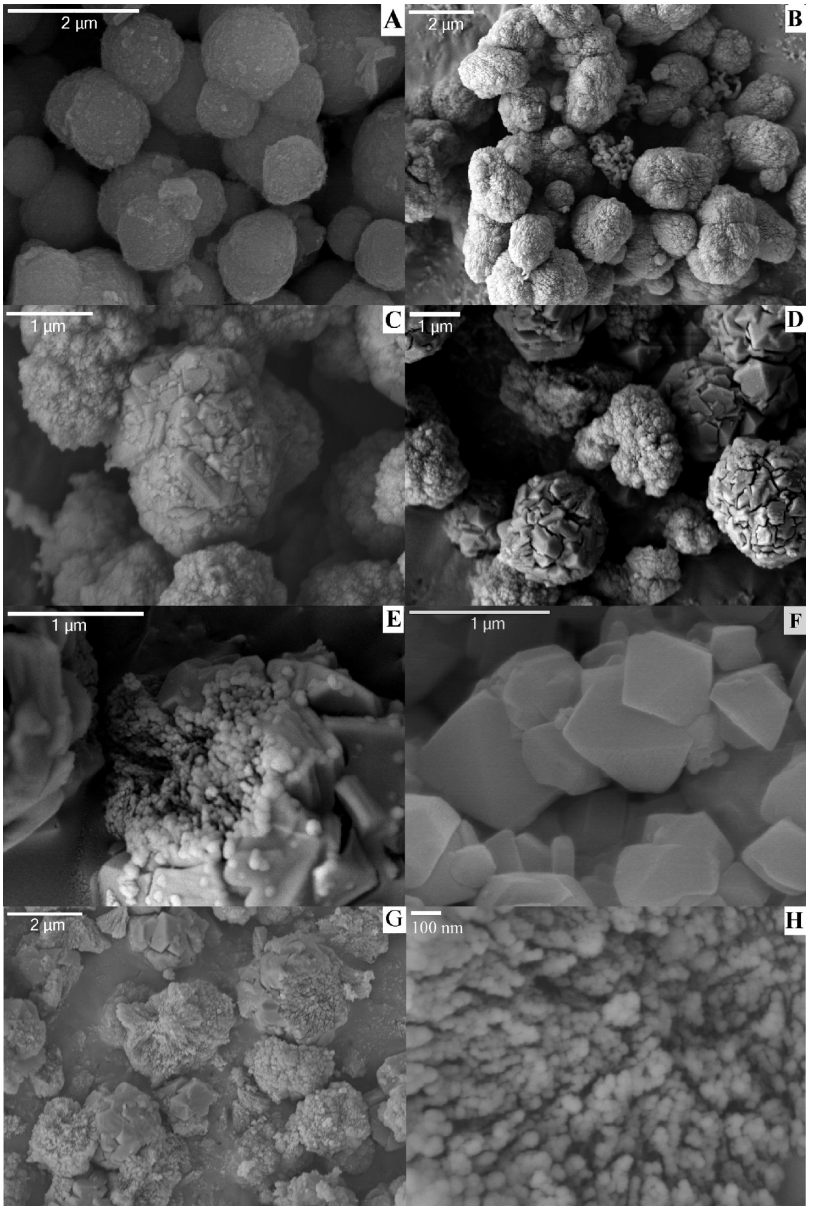

Figure 2. SEM images of the samples. (A) zeolite β; (B) BFZ-12; (C) BFZ-18; (D) BFZ-24; (E) BFZ-28; (F) zeolite Y; (G and H) sample BFZ-24 crushed by 3 MPa pressure.

It can be seen from Figure 2B that composite BFZ-12 has a rougher surface and larger crystal size than β-zeolite particles. However, octahedral crystal morphology of Y-zeolite cannot be observed despite of the coexistence of FAU and BEA zeolites phase in BFZ-12 suggested by the XRD pattern (Figure 1). As shown in Figure 3F, high resolution transmission electron microscopy (HRTEM) images of composite BFZ-12 show the shell an inconsecutive and interfluent micropores channel arrays, indicating the external surface of BFZ-12 a lower crystallization microstructure;[28] zeolite Y crystals accumulate and form the inconsecutive shell in the term of disorder. Figure 3F also confirms that the crystal particles in the shell have a relatively small size, which may not be detected by scanning electron microscopy (SEM).

When crystallization time was prolonged to 18 h, the morphology of composite BFZ-18 seems like rough spheres inlayed by many faujasite crystals with the sizes of about 100−200 nm (Figure 2C). When crystallization time was prolonged to 24−28 h, the zeolite composite shows a much more coarse surface. The faujasite particles in the shell have shown the distinctly octahedral characteristic with a small crystal size of 300−400 nm (Figure 2D,E). The steric hindrance provoked by the concurrently growing crystals in the shell is obviously the reason for the smaller size with respect to the crystals grown in the bulk.[29]

HRTEM images of zeolite composite BFZ-24 (Figure 3A) show the shell a uniform, well-ordered micropore channel array in large areas, indicating a highly crystallization microstructure.[28] The selected area electron diffraction (SAED)

(28) Liu, R.; Ren, Y.; Shi, Y.; Zhang, F.; Zhang, L.; Tu, B.; Zhao, D. *Chem. Mater.* **2008**, *20*, 1140.

(29) Bouizi, Y.; Rouleau, L.; Valtchev, V. P. *Chem. Mater.* **2006**, *18*, 4959.

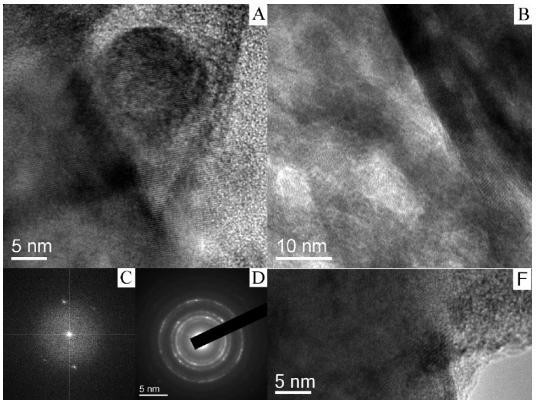

Figure 3. High resolution TEM images of the samples. (A) The shell layer zeolite in BFZ-24; (B) the core zeolite crystal in BFZ-24 crushed by 3 MPa pressure; (C and D) the corresponding SAED patterns of the shell layer and the core zeolites in BFZ-24; (F) the shell layer zeolite in BFZ-12.

pattern of the shell layer zeolites (Figure 3C) confirms that Y crystallites are indeed formed. Figure 3D shows the core zeolite a different SAED pattern from the shell layer zeolites, indicating that the core and the shell may be of different-type zeolite crystals. The chemical composition of a given zeolite is an important characteristic, which defines its properties.[30] EDS analysis of the silicon and the aluminum content shows the SiO_2/Al_2O_3 ratios of the shell and the core are 3.5 and 16.7, close to the 3.2 of Y-zeolite and the 18.5 of β-zeolites used in the experiments, respectively. It can be inferred from the above-mentioned results that the as-synthesized sample is a zeolite composite composed of β-zeolite crystal as the core and Y-zeolite crystals as the polycrystalline shell. Direct evidence for the presence of mesopores with a fairly uniform size of 8−10 nm in diameter is also provided by the TEM images as shown in Figure 3B.

The formation of core−shell zeolite−zeolite composites is a complex process and often controlled by more than one factor. As can be expected, chemical compatibility and overlapping of crystallization fields of the core and the shell materials is of great importance. Valtchev et al.[29,31] suggested that the chemical compatibility between core and shell materials and the match of crystallization conditions determined the formation of a core−shell composite. The incompatibility between the core crystals and the shell zeolite precursor mixture could be circumvented by the adsorption of nanoseed on the core surface, which induced the crystallization of the shell.[29,31] The difficulties of combining core and shell with substantially different compositions are obvious because the dissolution of the core material in the synthesis media leads to detachment of the seeds and probably to changes in chemical equilibrium at the solution−core crystal interface. Consequently, the conditions necessary for the secondary growth of the seed crystals cannot be obtained. Therefore, the secondary growth should surpass the dissolution so as to obtain a

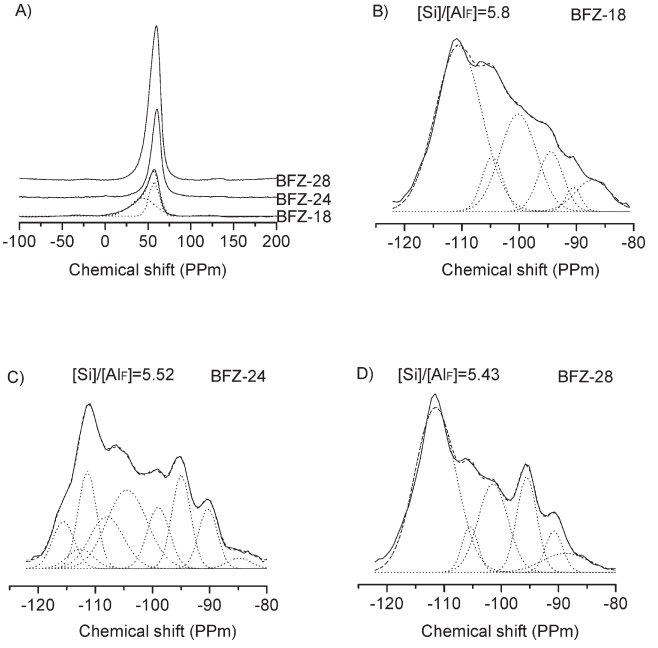

Figure 4. MAS NMR spectra of the calcined zeolite composites samples. (A) ^{27}Al MAS; (B, C, and D) ^{29}Si MAS.

rapid shell formation to protect the core. In this way, the core−shell zeolite−zeolite composite composed of β-zeolite core and Y-zeolite polycrystalline shell is very difficult to be obtained by the way of preliminary seeding of the shell nanoseeds on the core surface and subsequent secondary growth under hydrothermal conditions. Y-Zeolite is outside of the chemical compatibility and overlapping of crystallization fields of β-zeolite; dissolution is expected on some of the β-crystals due to the high alkalinity in the synthesis solution during the second-step synthesis.[13,27,30] Therefore, outside of the crystallization field of the given zeolite Y, the resulting shell formation is difficult.

In order to obtain the core−shell zeolite−zeolite composite composed of β-zeolite as the core and Y-zeolite as the shell, the effect of dissolution of the core on formation of the composite[27] should be taken into account, because dissolution of the core (zeolite β) will offer additional Si-rich species, that will change the chemical equilibrium at the interface between the core and the precursor mixture yielding the shell layer.[29] As a consequence, a modified synthesis procedure is required to acquire core−shell zeolite composite crystals with Y- and β-zeolites, which are incompatible with respect to the framework compositions and crystallizations. The silicon species extracted from the core zeolite crystals should be considered in advance and calculated in the formula of the precursor mixture yielding the shell layer zeolite. The strategy for synthesizing BFZ core−shell zeolite composite is that the silicon species of the precursor mixture of zeolite Y is obtained by extracting from β-zeolite crystals during the synthesis. Si-rich species extracted from β-zeolite will change the synthesis media and make the synthesis condition transforming to the crystallization field of Y-zeolite. During the second-step synthesis, the synthesis system lacks silicon species for Y-zeolite growth and the silicon

(30) Zheng, J.; Zhang, X.; Wang, Y.; Bai, Y.; Sun, W.; Li, R. *J. Porous Mater.* **2009**, *16*, 731.
(31) (a) Bouizi, Y.; Rouleau, L.; Valtchev, V. P. *Adv. Funct. Mater.* **2005**, *15*, 1955. (b) Bouizi, Y.; Majano, G.; Mintova, S.; Valtchev, V. P. *J. Phys. Chem. C* **2007**, *111*, 4535. (c) Bouizi, Y; Rouleau, L; Valentin, V. P. *Microporous Mesoporous Mater.* **2006**, *91*, 70.

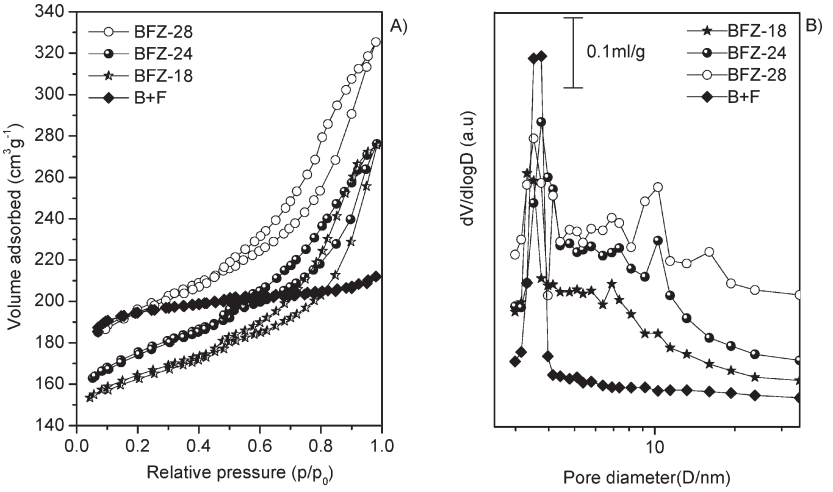

Figure 5. (A) N_2 adsorption−desorption isotherms and (B) the corresponding BJH pore size distribution curves.

species can only be obtained from the depolymerization of β-zeolite. The silicon extracted from β-zeolite reacts with the supplemented aluminum species, resulting in formation of the zeolite composite. Accurate feed calculation during the second-step synthesis, such as the matching of the supplemented aluminum and the extracted silicon and the adjusting of appropriate alkalinity as well as the controlling of crystallization temperature, makes the crystallization field for zeolite β transforming to zeolite Y and induces the crystallization of zeolite Y, resulting in the formation of Y-zeolite shell on β-zeolite. All these lead to on the one hand the formation of the composite zeolite and on the other hand the introduction of a mesopores system throughout the zeolite crystals. Therefore, β-zeolite crystal serves as the silicon source for the formation of Y-zeolite crystals as well as the core supporting the growth of Y-zeolite polycrystalline shell.[13]

Crystallization during the second-step synthesis induces considerable change in the coordination of silicon and aluminum atoms which composed the zeolite−zeolite composite framework, as shown in Figure 4A. As single Y- and β-zeolites, most of the silicon and aluminum atoms of composite BFZ-28 and BFZ-24 are tetrahedrally coordinated, confirming their high crystallinity. At the preliminary stage during the second-step synthesis, the peak located at 55 PPm of BFZ-18 shows a dissymmetrical peak, which can be fitted by two peaks of 40 PPm and 60 PPm, respectively, indicating the presence of partial nonframework aluminum in BFZ-18. With the crystallization time increasing, the peak located at 55 PPm in the ^{27}Al MAS NMR spectrum of BFZ-18 shifts to 58 PPm of BFZ-24 and to 60 PPm of BFZ-28, and the peak strength correspondence to tetrahedrally coordinated aluminum becomes strong. That shows the composite zeolites a variable aluminum environment, and the nonframework aluminum species gradually enter the framework of Y-zeolite with the increase of crystallization time during the second-step synthesis.

The SiO_2/Al_2O_3 of BFZ-24 determined by EDS analysis shows from the core to the shell direction a trend of increasing first and then decreasing, namely, from 16.7 of the core to 23.3, 76.9, 28.8, and 3.49 of the shell, indicating there is a transport course of components (Si-species) from the core to the growing shell during the zeolite composite formation, which is in good agreement with the results observed by Valtchev et al.[29,31] Zeolite framework Si/Al ([Si]/[Al_F]) ratios were obtained from the corresponding deconvoluted ^{29}Si MAS NMR spectra (Figure 4) by calculating according to the method reported in the literature.[32] With crystallization time increasing, only a slight decrease of the [Si]/[Al_F] value in zeolite composite was observed (Figure 4B−D). The [Si]/[Al_F] value of the composite decreased from 5.80 in BFZ-18 to 5.52 in BFZ-24 and then to 5.43 in BFZ-24. In theory, the extraction of silicon from β-zeolite crystals should lead to a distinct drop in the [Si]/[Al_F] value with increasing crystallization time during the second-step synthesis. It can be inferred from the results that most of the extracted silicon from β-zeolite has been transferred to the framework of Y-zeolite crystals; the formation of the shell layer also prevents excessive silicon extraction from the core,[29] resulting in a relatively stable value of [Si]/[Al_F] in composite samples.

With Si extraction from the core, the related mesopore formation[11−13,17−19] occurred in β-zeolite crystals. Zeolite composite BFZ-24 was crushed by 3 MPa pressure so as to discover its nature structure, as shown in Figure 2G, H. The cores are partially exposed due to partial damage of Y-zeolite polycrystalline shell. A considerable number of pinholes can be obviously observed in the core (Figure 2H). Groen et al.[11,12,20] suggested that Al gradient would affect and control the Si extraction throughout the zeolite particles. A high framework Al concentration prevents Si extraction, while a low Al concentration leads to excessive extraction and formation of large pores.[20] The presence of an aluminum-poor interior and an aluminum-rich outer rim in β-zeolite crystals results in Si extraction favorably occurring in the aluminum-poor bulk rather than the aluminum-rich external surface.[13] Subsequent alkaline treatment of β-zeolite crystal during the second-step synthesis will result in a preferential dissolution

(32) Xie, Z.; Chen, Q.; Chen, B.; Zhang, C. *Cryst. Eng.* **2001**, *4*, 359.

Table 1. Characteristics of Zeolite Composite BFZ

samples	S_{BET} (m^2/g)	S_{micro} (m^2/g)	S_{meso} (m^2/g)	V_{micro} (cm^3/g)	V_{meso} (cm^3/g)	L/B (Py)	acidity (Py)[b], mmol/g		k_1[c]	HF[d]
							Brönsted	Lewis		
BFZ-28	604	448	130	0.23	0.25	1.23	0.453	0.557	1.26	0.104
BFZ-24	580	441	101	0.22	0.21	0.94	0.432	0.406	0.92	0.089
BFZ-18	507	392	102	0.20	0.19	0.69	0.417	0.291	1.15	0.102
B + F[a]	608	492	36	0.25	0.04	1.04	0.494	0.515	0.49	0.051
BEA	517	367	29	0.18	0.04	0.43	0.503	0.215	0.31	0.045
FAU	738	701	9	0.36	0.02	1.92	0.480	0.924	0.81	0.012

[a] B + F is the corresponding physical mixture of Y and β-zeolites with the same weight percent of Y-zeolite and similar Si/Al ratio as zeolite composite BFZ-28. [b] C(pyridine on B sites) = 1.88IA(B)R^2/W; C(pyridine on L sites) = 1.42IA(L)R^2/W (the formulas are from ref 42); pyridine desorption was performed at 573 K. [c] The rate constants. [d] The hierarchy factor (HF) is determined as the product (V_{micro}/V_{pore}) × (S_{meso}/S_{BET}) (see reference 38).

of the aluminum-poor center and the formation of hollow crystals with a relatively preserved outer surface.The preserved external surface supports the shell layer of Y-zeolite growing, resulting in the formation of the core−shell zeolite−zeolite composite. The external surface of β-zeolite crystal plays an important role for the formation of polycrystalline shell. Y-zeolite seeds are first adsorbed and deposited on the external surface of β-crystal due to its higher surface area.[33]Second, the seeds begin growing because of the interaction between the aluminum species in the solution and the silicon species extracted from β-zeolite crystals, resulting in the formation of Y-zeolite polycrystalline shell around β-zeolite particles.

The adsorption−desorption of nitrogen on the mixture B + F is a type-I isotherm (Figure 5A), indicating the presence of micropores only. However, a curve combining type-I and type-IV isotherms is observed for BFZ. A larger hysteresis loop occurs after $p/p_0 \approx 0.45$ in the adsorption−desorption isotherm of the zeolite composite, which most probably relates to space filling in grain boundaries from the shell layer or pinholes in the core zeolites. Moreover, significant increase in N_2 adsorption is also observed from $p/p_0 \approx 0.8$ for composite BFZ. According to the SEM/HRTEM results mentioned above, larger pores have been created in the zeolite composite. The sharp condensation in the range of $p/p_0 \approx 0.8-1.0$ should, therefore, be attributed to the filling and emptying of mesopores by capillary condensation.[34]

Groen et al.[11,12] found that the loss of silica by alkali treatment induces a significant change in the pore structure of MFI zeolite. The alkaline-assisted hydrolysis of the Si−O−Si bonds from the zeolite framework was directed toward mesoporosity development.[2] As shown in Figure 5B, the pore size distribution of composite BFZ-18 illustrates the existence of a mesopore structure with pore size centered around 3.7 and 6.9 nm; a mesopore structure with pore size centered around 3.7, 6.9, and 10.3 nm is presented in composite BFZ-24; another mesopore structure with pore size centered around 16 nm is introduced in composite BFZ-28. However, the BJH pore size distribution derived from the adsorption branch of the isotherm does not show the similar distribution in the physical mixture B + F. The pores centered around 6.9, 10.3, and 16 nm can be attributed to the enlargement of micropores resulting from the contribution of silicon extracted from β-zeolite, which is in good agreement with the results in the literature.[11−13,35,36]

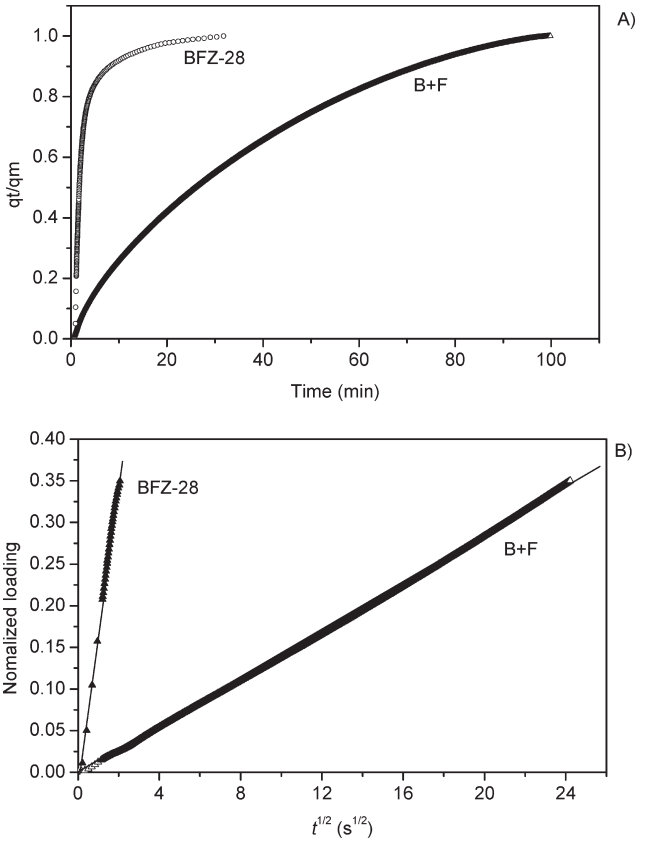

Figure 6. Adsorption kinetics curves of isopropylbenzene over physical mixture B + F and zeolite composite BFZ, $p/p_0 = 0.015$. (A) Isopropylbenzene uptake curves of the zeolite composite BFZ and the physical mixture B + F. (B) Uptake profiles in a short time domain. Straight lines correspond to fitting by eq 2.

Some data of N_2 adsorption−desorption is presented in Table 1. The value of the BET surface area of zeolite composite BFZ-28, BFZ-24, and BFZ-18 are 604, 580, and 507 m^2/g, respectively, lower than the 608 m^2/g of the mixture B + F. The decrease of BET surface area is most probably because of the dissolution of β-zeolite, which results in the breakdown of part micropores.[27] A decrease

(33) Dutta, P. K.; Bronic, J. *Zeolites* **1994**, *14*, 250.
(34) Bjørgen, M.; Joensen, F.; Holm, M. S.; Olsbye, U.; Lillerud, K.-P.; Svelle, S. *Appl. Catal., A: Gen.* **2008**, *345*, 43.
(35) Groen, J. C.; Jansen, J. C.; Moulijn, J. A.; Pérez-Ramírez, J. *J. Phys. Chem. B* **2004**, *108*, 13062.
(36) Jung, J. S.; Park, J. W.; Seo, G. *Appl. Catal., A: Gen.* **2005**, *288*, 149.

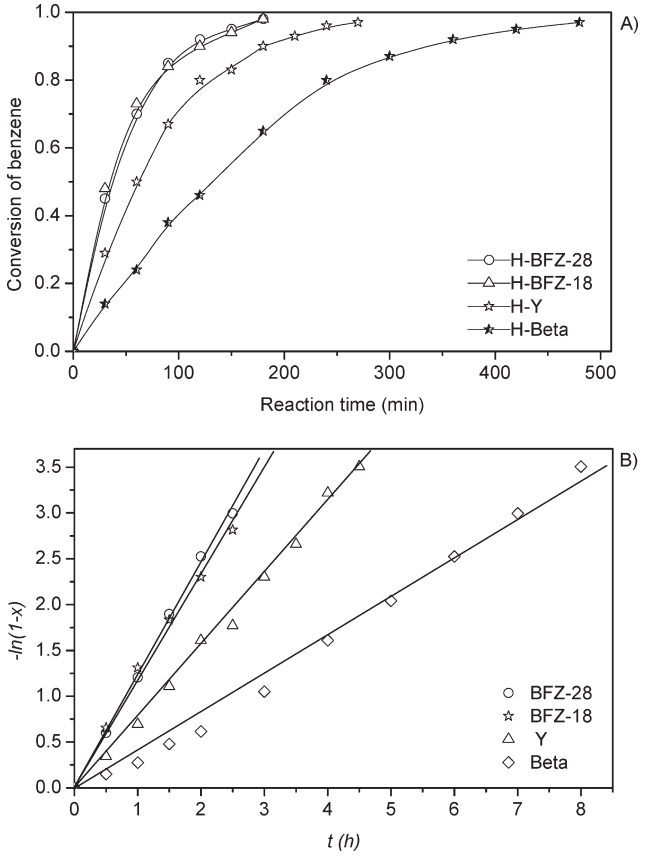

Figure 7. Liquid-phase hydrogenization of benzene over Ru/H-BFZ, Ru/H-Y, and Ru/H-β. (A) Benzene conversion as a function of reaction time over various supported Ru catalysts. (B) Straight lines correspond to fitting by the equality of $-\ln(1 - x) = k_1 t$.

to the nanocrystalline region for Y-zeolite particles in the shell may also play a role, which causes the deterioration of the ordering of the three-dimensional network.[6] However, the mesoporous surface area and mesoporous volume of the composite BFZ are much larger than those of the physical mixture B + F. The mesoporous volume of composite BFZ-28 is 0.25 cm^3/g, which is about 6 times higher than the 0.04 cm^3/g of the corresponding physical mixture.

Compared with the physical mixture H-(B + F), composite H-BFZ-28 has relatively more Lewis acid sites and less Brönsted acid sites. The ratio of Lewis to Brönsted acid sites in H-BFZ-28 is about 1.23, larger than the 1.04 in H-(B + F) (Table 1). As shown in Figure 2, the crystal size of Y-zeolite in the polycrystalline shell is smaller than that of Y-zeolite in the corresponding physical mixture. Smaller crystal size brings a decrease in protonic acidity and a significant increase in Lewis acidity. The relatively more Lewis acidity can also be ascribed to the destruction of some Si−O−Si and Si−O−Al bonds in β-zeolite and the formation of additional AlOH groups during the composite synthesizing.[27]

3.2. Isopropylbenzene Diffusion. The creation of mesopores in zeolite crystals is equivalent to increasing the external surface area of the zeolite, in this respect a larger number of pore windows is made accessible to the reactants. To verify the improved transport properties of the core−shell BFZ crystals, we selected isopropylbenzene as a probe to make a comparative study on the uptakes in the composite and the corresponding mixture samples. The relatively large molecular size of isopropylbenzene, which is similar to the channel openings of Y and β, allows an accurate assessment of the uptake rates.

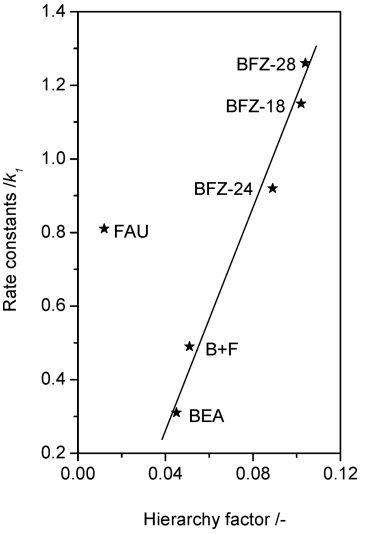

Figure 8. Relationship between the hydrogenation activity (the rate constants) and the HF (hierarchy factor) of the different catalysts.

As expected, the isopropylbenzene uptake in the mixture is extremely slow (Figure 6A). Approximately 55 min are required to reach 80% of the maximum uptake. Contrary, the uptake rate of isopropylbenzene in the composite is greatly enhanced, especially in the initial stage where the uptake is sharply increased and a similar uptake of 80% is achieved only after 4 min. From the view of Groen et al.[12] that mesopores created in ZSM-5 zeolite crystals did not change the micropore properties in terms of adsorption and diffusion, the intrinsic diffusivity of isopropylbenzene in the micropores should be the same either in the composite zeolite or in the corresponding physical mixture samples. Therefore, the enhanced uptake rate of isopropylbenzene in the composite must be attributed to an improved accessibility and a shorter diffusion path length in the micropores resulting from an accessible network of mesopores observed by SEM/HRTEM and N_2 adsorption−desorption.

Further quantification of the diffusion properties in the different zeolite crystals was attained using Fick's second law, which describes the change of the concentration of molecules inside the zeolite crystals as a function of time

$$\frac{\partial C}{\partial t} = D\frac{\partial^2 C}{\partial x^2} \tag{1}$$

During the initial stage of uptake in the samples, the following appropriate solution applies:

$$\frac{q(t)}{q(m)} = \frac{6}{\sqrt{\pi}}\sqrt{\frac{D}{r^2}}\sqrt{t} \tag{2}$$

where $q(t)/q(m)$ is the normalized loading, D is the diffusivity, r is the characteristic diffusion length, and

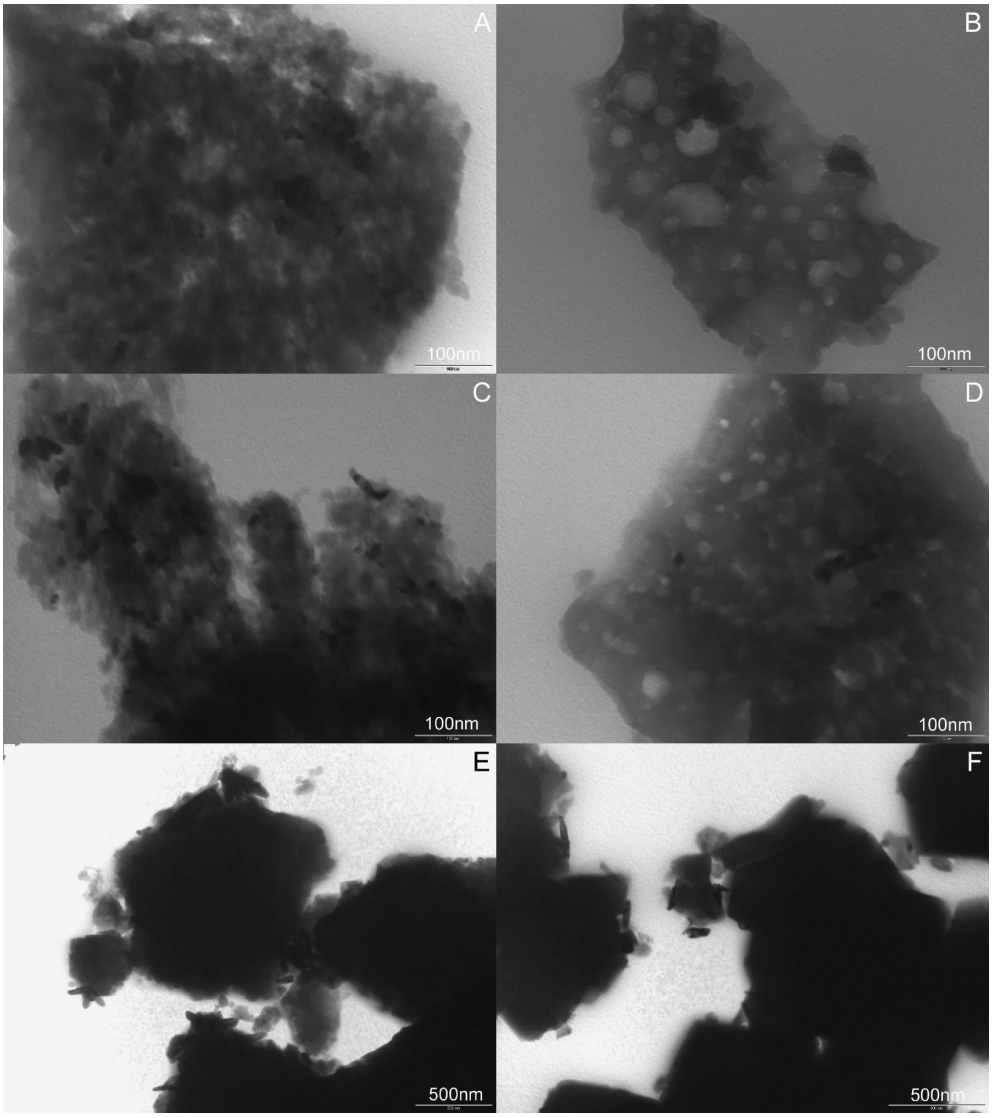

Figure 9. High resolution TEM images of the samples supported metallic ruthenium. (A, B) Ru/H-BFZ-18; (C, D) Ru/H-BFZ-28; (E) Ru/H-β; (F) Ru/H-Y. The metallic ruthenium supported over the samples was reduced under H_2 atmosphere prior to TEM analyses.

t is time.[37] The characteristic diffusion length r of the crystals in the physical mixture was derived from high-resolution SEM and estimated at 0.5 μm. Plotting the normalized loading versus the square root of time for the samples leads to a straight line, as shown in Figure 6B. This fitting leads to a characteristic diffusion time of $r^2/D = 5.5 \times 10^4$ *s*. Combined with $r = 0.5$ μm, a diffusivity D of approximately 4.6×10^{-18} m^2s^{-1} is obtained. Since the diffusivity in the micropores of both the composite and the corresponding physical mixture is the same,[12] the isopropylbenzene uptake curve over the physical mixture can then be used to estimate the characteristic diffusion length in the BFZ zeolite. The characteristic diffusion time has been determined during the initial uptake up to $q(t)/q(m) = 0.5$, where a straight line has been obtained (Figure 6B). This provides an average characteristic diffusion time of 4.0×10^2 s, which is more than 2 orders of magnitude shorter than in the corresponding physical mixture. The resulting characteristic diffusion length is 4.3×10^{-2} μm and accounts for ca. 50% of the total uptake.

3.3. Liquid-Phase Hydrogenation of Benzene. The catalysis of the composite H-BFZ supported by 3 wt % Ru was investigated during the liquid-phase hydrogenation of the 0.06 wt % benzene/hexane model reactant and compared with those of H-Y- and H-β-zeolites supported by the same Ru loading. The conversion−time curves obtained under the same reaction condition on Ru/H-Y, Ru/H-β, Ru/H-BFZ-18, and Ru/H-BFZ-28 were depicted in Figure 7A. The concentration of benzene in solution is gradually decreased to 5 ppm, because of hydrogenation of benzene into cyclohexane over the catalysts. In order to compare the activity of the different catalysts based on the kinetic rate constants for the process, the experimental data of conversion (x) − time (t) is fitted, as shown in Figure 7B. It is found that the relation can match the following first-order kinetic equation well:

$$-\ln(1-x) = k_1 t$$

(37) Ruthven, D. M.; Brandani, S.; Eic, M. *Molecular Sieves Science and Technology-Adsorption and Diffusion*; Karge, H. G., Weitkamp, J., Eds.; Springer: Berlin, 2008; Vol. *2*, Chapter 2.

According to this equation, the rate constants (k_1) are 1.26, 1.15, 0.81, and 0.31 h^{-1} for Ru/H-BFZ-28, Ru/H-BFZ-18, Ru/H−Y, and Ru/H-β-catalysts, respectively. Apparently, composites supported catalysts show their superior hydrogenation activity. The higher activity observed for H-BFZ supported catalysts can be explained by the introduction of the hierarchical pore system.

Pérez-Ramírez et al.[38] put forward a conception of HF (hierarchy factor) and found it an appropriate tool to classify hierarchically structured materials. The relationship between the hydrogenation activity and the hierarchy factor of the different samples (purely microporous and hierarchical) has been plotted and is shown in Figure 8. Except for Ru/H-Y, the rate constants of liquid-phase hydrogenation over the Ru supported catalysts show a linear dependence with the hierarchy factor. The hydrogenation performance of the hierarchical zeolite composite BFZ is better than that of the purely microporous zeolite (Y, β, and the corresponding physical mixture). The benefit of improved transport in the composite catalysts is, therefore, more influential than the loss of microporosity, and the net effect still results in an improved catalytic performance. As compared with β-zeolite, Y-zeolite has a higher hydrogenation activity despite a lower HF, which can be ascribed to its larger micropore channels. More acid sites and, therefore, the supply of extra active sites for the hydrogenation reaction may also bring H-Y catalyst a higher activity than the H-β supported catalyst.

The higher activity observed for H-BFZ supported catalyst can also be ascribed to the enhanced Ru dispersion. The results decided by TEM (Figure 9) show that metallic ruthenium particles on the hierarchical porous zeolite composite have a much smaller particle size as compared with those on the purely microporous FAU and BEA zeolites. TEM analyses also showed that the metallic ruthenium particles were only situated on the external surface of the purely microporous Y- or β-zeolites. However, only a trace of metallic ruthenium particles was observed on the external surface of zeolite composite, and most of metallic ruthenium particles were found in the mesopores of the hierarchical composite. The aforementioned result indicates that the presence of the hierarchical porous system in the composite zeolites brought an enhanced Ru dispersion. It is known that aromatic hydrogenation can occur on both metallic sites and acid sites close to the metal particles implying spillover of hydrogen from the metal surface or the metal−support boundary.[39,40] The enhanced Ru dispersion supplies an extra metal surface available for benzene conversion and the hydrogen dissociation on the metal, which increases hydrogen spillover.

In addition, the higher hydrogenation activity on zeolite composite Ru/H-BFZ could also be caused by both improved transport of the reactants to and from the active sites in its channel and higher acid site accessibility resulting from the existence of the mesopores.[41] The diffusion times of isopropylbenzene over Ru/H-(B + F) and Ru/H-BFZ-28 were 9.9×10^4 and 1.3×10^3 s, respectively, longer than the 5.5×10^4 and 4.0×10^2 s over B + F and BFZ-28, respectively. Higher diffusion limitation in the supported catalysts as compared with in the no-loaded samples can be caused by the pore blockage effects. However, a more than 70 times shorter diffusion time than that in the Ru/H-(B + F) can still be obtained in the Ru/H-BFZ-28.

4. Conclusions

In summary, a hierarchical porous zeolite composite BFZ has been synthesized using β-zeolite as silica sources as well as the core supporting the shell Y-zeolite growing. The synthesis strategy during the second-step synthesis design makes the silica-source rule a more advantageous approach to prepare core−shell structure zeolite−zeolite composite for the incompatibility of chemical compositions and the crystallization conditions between the core crystals and the shell zeolite precursor mixture as compared to the classical preliminary seeding on the core surface. A mesopore structure with pore size centered around 6.9, 10.3, and 16 nm was created in the composite due to the extraction of silicon from the core. As a result, the characteristic diffusion path length in the composite zeolite crystals is dramatically shortened, resulting in an approximately 2 orders of magnitude faster diffusion of isopropylbenzene in the micropores as compared to the corresponding physical mixture. The presence of the hierarchical porous system in the composite zeolites ena bles more rapid molecular transport and more accessible acid sites and also brings an enhanced Ru dispersion. The improved gas transport properties and accessible acid sites as well as enhanced Ru dispersion give the catalyst a higher activity.

Acknowledgment. This work is supported by the "973" project (No. 2005CB221204) and SinoPEC (No. 107009).

(38) Pérez-Ramírez, J.; Verboekend, D.; Bonilla, A.; Abelló, S. *Adv. Funct. Mater.* **2009**, *19*, 3972.
(39) Lin, S. D.; Vannice, M. A. *J. Catal.* **1993**, *143*, 563.
(40) Simon, L. J.; van Ommen, J. G.; Jentys, A.; Lercher, J. A. *Catal. Today* **2002**, *73*, 105.
(41) Zheng, J.; Zhang, X.; Zhang, Y.; Ma, J.; Li., R. *Microporous Mesoporous Mater.* **2009**, *122*, 264.
(42) Emeis, C. A. *J. Catal.* **1993**, *141*, 347.